

Topological superconductivity in a topological insulator

Hao Yu^{1,2,5}, Noah F. Q. Yuan^{1,5}, Wei-Jian Li^{3,2}, Liu-Cheng Chen^{1,2}, Zi-Yu Cao¹, Di Li⁴, Xiaoying Qin⁴, Chang-De Gong³ & Xiao-Jia Chen^{1,2*}

¹*School of Science, Harbin Institute of Technology, Shenzhen 518055, China*

²*Center for High Pressure Science and Technology Advanced Research, Shanghai, 201203, China*

³*National Laboratory of Solid State Microstructures and School of Physics, Nanjing University, Nanjing 210093, China*

⁴*Key Laboratory of Materials Physics, Institute of Solid State Physics, Chinese Academy of Sciences, Hefei 230031, China*

⁵*These authors contribute equally to this work.*

**E-mail: xjchen2@gmail.com*

Topological superconductivity as an exotic quantum phenomenon with coupled nontrivial topological order and superconductivity together in a single substance has drawn extensive attention because of its novelty as well as the potential for quantum computation¹⁻⁶. A direct idea for producing topological superconductors is to create superconductivity based on the well recognized topological insulators⁷⁻¹⁴. The topological insulating states in highly efficient thermoelectric materials Bi_2Te_3 and Bi_2Se_3 and their alloy $\text{Bi}_2\text{Te}_{3-x}\text{Se}_x$ have been established from angle-resolved photoemission¹⁵⁻¹⁷ and transport¹⁸ experiments. Superconductivity was also observed based on these popular topological insulators by the application of pressure¹⁹⁻²¹, chemical dopant²², and heterostructures^{23,24}. However, the experiments

mainly focusing on Bi_2Se_3 doped by metals such as Cu^{25–35}, Sr^{36–39}, and Nb^{40–46} have not provided the consistent evidence to support the topological superconductivity. Here we carry out a systematic high-pressure study on a topological insulator $\text{Bi}_2\text{Te}_{2.7}\text{Se}_{0.3}$ to provide the convincing evidence for the expected topological superconductivity. Four phases with different structures are found upon compression by the X-ray diffraction, Raman scattering, and electrical transport measurements. The Hall resistivity and electronic structure calculations help to identify the topological surface state in the entire initial phase, while superconductivity is found to coexist with such a state of the compressed material after its passing the electronic topological transition, followed by three other superconducting phases without topological character. For these superconducting phases, we observe that the upper critical field follows with the temperature in the critical exponent $2/3$ for the first one with the topological surface state and 1 for the left. These observations support the realization of the topological superconductivity in the initial phase according to the theoretically proposed critical field measure. Therefore, this work points out a big pool and new direction for finding topological superconductors from topological thermoelectric materials. The results also demonstrate that the critical field measure is an easy and powerful method for the identification of topological superconductivity in the system where topological surface states and superconductivity coexist.

Symmetry and topology are two of the main themes of modern physics, especially the condensed matter physics in recent decades. In two dimensions (2D), quantum (anomalous) Hall effects emerge with nontrivial electronic topology when the time-reversal symmetry is broken⁷. When the time-reversal symmetry is preserved, quantum Hall states then develop into the quantum

spin Hall (QSH) phase^{8,9}. In three dimensions (3D), stacked QSH states evolve into topological insulators (TIs)¹⁰⁻¹². The crystal symmetries further intertwine with the electronic topology, leading to topological crystalline insulators⁴⁷⁻⁴⁹. These topological insulating phases have been experimentally verified with high precision in several materials, in particular highly efficient thermoelectric materials Bi_2Te_3 and Bi_2Se_3 and their alloy $\text{Bi}_2\text{Te}_{3-x}\text{Se}_x$ ¹²⁻¹⁸. Importantly, such TI materials have also been found to be intrinsically superconducting by the application of pressure¹⁹⁻²¹ or chemical dopant^{22,36,37,40,41}, which naturally invites two questions on the nature of this kind of superconductivity. From the symmetry wise, one needs to determine the pairing symmetry of the intrinsic superconductivity. From the topology wise, one needs to know whether and how the topological superconductivity can be realized in these topologically nontrivial materials.

Theoretical proposals followed by various experimental measurements have been carried out to address these two questions. Classified by the irreducible representations of the point group D_{3d} , the possible pairing symmetry of Bi(Te,Se) systems has been theoretically proposed as A_{1g} phase (s -wave), odd-parity A_{1u} phase³¹⁻³³ or two-component E_u phase (nematic^{34,35} versus chiral⁴²). For doped topological insulators, some experimental data support the A_{1g} phase (s -wave)²⁷ without topological superconductivity³⁰ for Cu-doped Bi_2Se_3 , while others support the nematic E_u phase for Bi_2Se_3 doped with Cu^{26,28,29}, Sr³⁶⁻³⁹ or Nb^{41,43-46}, which are believed to host topological superconductivity, although discrepancy still remains^{35,46}. For topological insulators under pressure, experimental data indicate unconventional superconductivity in Bi_2Se_3 ²¹, while no direct evidence on unconventional superconductivity has been provided in Bi_2Te_3 ²⁰. The issue regarding whether topological superconductivity can take place in topological insulators has not been settled yet but

is highly desired from the science community. To address this issue, we conduct a careful experimental and theoretical study on both the normal phase and superconducting phase of $\text{Bi}_2\text{Te}_{2.7}\text{Se}_{0.3}$ at high pressures. The details are given as follows.

The room-temperature phase and structure behaviours of $\text{Bi}_2\text{Te}_{2.7}\text{Se}_{0.3}$ at ambient pressure and high pressures were determined by X-ray diffraction measurements. The details for the experiments and refinements are given in Methods. The diffraction patterns and profiles indicate the occurrence of several phases at high pressures (Fig. 1a). The Rietveld refinements for four representative pressures yield good agreement between the measurements and calculations (Fig. 1b). The obtained structural parameters are summarized in Extended Data Table 1. The results support the formation of three new phases besides the initial one. All the obtained phases are named as I to IV with space groups of $R\bar{3}m$, $C2/m$, $C2/c$, and $Im\bar{3}m$ from the ambient to high pressure, respectively. The evolution of the volume per formula of these phases and the atomic arrangements for Bi and Te(Se) in each structure are presented in Fig. 1c. Phase I can maintain its initial rhombohedra structure up to 10 GPa. For Phase IV, all three kinds of atoms could occupy the same position with equal possibility and are hence geometrically indistinguishable. The obtained phases and structures of $\text{Bi}_2\text{Te}_{2.7}\text{Se}_{0.3}$ are consistent with the previous studies on the two ending compounds Bi_2Te_3 ⁵⁰ and Bi_2Se_3 ⁵¹. Interestingly, the axial ratio c/a of the lattice parameters exhibits non-monotonic behaviour under pressure with a minimum at around 2 GPa (Fig. 1d). Such a minimum was also observed in both Bi_2Te_3 ⁵² and Bi_2Se_3 ⁵¹. It has been proposed to be associated with the Lifshitz transition, also known as the electronic topological transition (ETT)⁵². The experimental evidence for pressure-induced ETT in $\text{Bi}_2(\text{Te,Se})_3$ -based system through vari-

ous techniques is summarized in Methods. For *n*-type Bi₂Te_{2.7}Se_{0.3}, the ETT near 2 GPa has been firmly confirmed through the pressure dependence of σ , S , their power factor σS^2 , effective mass, and charge mobility⁵³.

The structural characters of the obtained four phases were further examined through high-pressure Raman scattering measurements. The phonon modes appear in accordance with the structural symmetry of each phase (Extended Data Figs. 1a and 1b). For example, the *R-3m* symmetry predicts four phonon modes for the first phase (I)⁵⁴. We do observe these modes in the pressure range up to 8 GPa. The pressure dependence of the low-frequency E_g^1 mode is the first report in history^{51,54}. The flat background at high pressures is just the feature of Phase IV with space group of *Im-3m* because no active Raman modes are expected from the symmetry consideration. The details for the mode assignment are given in Methods. The pressure dependence of the frequencies of the obtained phonon modes provide the accurate boundaries between phases and their coexistence (Extended Data Fig. 1c). Note that the slope change of the pressure-dependent frequency can be observed at around 2 GPa for all the phonon modes in Phase I. Meanwhile, the full width at half maximum (FWHM) has the maximum (minimum) for the E_g^1 (E_g^2) mode at pressure near 2 GPa where the FWHM of the A_{1g}^1 and A_{1g}^2 mode changes slope (Extended Data Fig. 1d). These offer additional spectroscopic evidence for the ETT in Phase I of the studied material.

Hall effect measurements at low temperature of 10 K were carried out to examine the validity of the nontrivial topological surface states under pressure. The Hall resistivity ρ_{xy} vs magnetic field curves for representative pressures reveal the different nature of the carriers in the obtained four

phases (Fig. 2a). The first phase (I) and the last two phases (III and IV) hold the n -type feature, while Phase II becomes a p -type material. This indicates that the electrical transport properties of the two intermediate phases (II and III) are controlled by the different types of the carriers. The robust topological order in $\text{Bi}_2\text{Te}_{3-x}\text{Se}_x$ has been reported from the angle-resolved photoemission measurements¹⁷. The Hall conductivity data of Phase I at various pressures exhibit a nonlinear resonant structure when applying magnetic fields (Extended Data Fig. 2), evidencing the existence of the surface state in topological insulators¹⁸. The Hall conductivity can be decomposed into the surface and bulk components based on the method developed recently¹⁸. The details for determining the mobility of the surface μ_s and bulk μ_b state as well as the carrier concentration n of the bulk are described in Methods. Fitting our experimental data yields the Hall conductivity for the surface σ_{xy}^s and the bulk σ_{xy}^b , supporting the existence of the nontrivial topological states in Phase I (Fig. 2b and Extended Data Fig. 2). However, the topological states does not survive in the rest three high-pressure phases reflected from the absence of the resonant structure of the Hall conductivity.

The obtained surface mobility μ_s is one order larger in magnitude than the bulk value μ_b over the whole pressure region studied in Phase I, supporting the nontrivial topological state. As can be seen from Fig. 2c, both mobilities increase with increasing pressure. The bulk one reaches a maximum at the boundary between Phase I and II. The mobility decreases with increasing pressure in Phase II. There is a minimum at the boundary between Phase III and IV. The distinct phase boundaries can be clearly established from the pressure dependence of the effective carrier concentration n_{eff} for the bulk state in Phase I and the Hall concentration n_H in the rest three phases (Extended Data Fig. 3). These boundaries seemingly do not shift with temperature when keeping pressure

unchanged. Now the phases and their boundaries are well determined for $\text{Bi}_2\text{Te}_{2.7}\text{Se}_{0.3}$ from X-ray diffraction, Raman scattering, and Hall effect measurements.

We perform the first-principles calculations of the $\text{Bi}_2\text{Te}_{2.7}\text{Se}_{0.3}$ alloy in the $R\bar{3}m$ phase under pressures (Fig. 3a). For the chosen first Brillouin zone and the projection along the (001) surface (Fig. 3b), the metallic surface state appears in all the pressure range studied up to 8 GPa (Fig. 3c), in good agreement with the transport measurements at temperature of 10 K (Fig. 2b). Furthermore, the evolution of energy contours of the top bulk valance band with increasing pressure (Fig. 3d) indicates the ETT around 2 GPa, where energy contours merge together and the number of distinct contours at the same energy changes from 3 to 2 as pressure increases. The numerical result of ETT is consistent with the transport and Raman scattering measurements.

Among the obtained four phases, only Phase I carries on the topological states at room temperature. Therefore, topological superconductivity can be only expected in this phase. To verify this expectation, we then cool down the material and perform transport measurements.

As expected, superconducting transitions are observed at low temperatures with a sudden resistivity drop at 4.3 GPa and even to zero value at 5.5 GPa, and the zero-resistivity states are always achievable for pressures higher than 5.5 GPa (Fig. 4a) within the experimentally achievable pressure range. The suppression of superconductivity by the applied magnetic fields is demonstrated in Fig. 4b for selected pressures of interest. The superconducting phase diagram in the pressure-temperature plane is presented in Fig. 4c. A comparison of the present results with the other experiments is given in Methods.

The same spectroscopic features at room temperature (Extended Data Fig. 1), low temperature of 3.6 K (Extended Data Fig. 4), and the temperatures across T_c (Extended Data Fig. 6) indicate that the compound keeps the same electronic phases at low temperatures as determined at room temperature. The nontrivial topological states can coexist with the superconducting state in Phase I at pressures up to 10 GPa (Extended Data Fig. 4). This topological state maintains when the material enters the superconducting state (below T_c) (Extended Data Fig. 6). In other words, among the obtained four superconducting phases, the superconducting state in Phase I is the only one to coexist with the nontrivial topological states in the studied compound. Therefore, the region at pressures of 5.5-10 GPa and temperatures less than T_c in Phase I provides the only window to examine the possibility of topological superconductivity in $\text{Bi}_2\text{Te}_{2.7}\text{Se}_{0.3}$.

Now we turn to the identification of the coexistence between superconductivity and topological surface states by investigation of critical fields in the Ginzburg-Landau regime near T_c . In Fig. 4b, two distinct types of critical fields have been obtained. In the three high-pressure phases (II, III, IV) without the topological surface states, the linear temperature dependence $H_{c2} \propto 1 - T/T_c$ is found, while in Phase I it can be found that $H_{c2} \sim (1 - T/T_c)^{2/3}$ near T_c (Inset of Fig. 4b and Extended Data Fig. 5). This sharp contrast is in excellent agreement with the theoretical prediction of the critical fields in trivial versus topological superconductors. To understand this mechanism, we need to work out the order parameter and the critical field by minimizing Ginzburg-Landau free energy, as elaborated in Ref.⁵⁵. In the following we stretch the outline of the theory.

In the trivial superconductors without surface states, the critical field is linear in temperature.

Denote $\xi \propto (1 - T/T_c)^{-1/2}$ as the coherence length of the superconductor, then superconductivity is killed when a flux quantum $\Phi_0 = h/(2e)$ is trapped in the area $\sim \xi^2$. As a result, $H_{c2} \propto 1/\xi^2 \propto 1 - T/T_c$, which corresponds to the high-pressure cases as shown for 14.0 GPa and 16.8 GPa (Fig. 4b and Extended Data Fig. 5).

In the topological superconductors with surface states, the critical field can have critical exponent of $2/3$ in the temperature dependence. After the bulk superconductivity is killed, as we further increase magnetic field strength, the surface layer of the thickness $\sim l_s$ prefers to remain superconducting. The new length scale l_s , known as the extrapolation length, measures the coupling strength between the topological states and superconductivity on the surface. When a flux quantum is trapped in the area $\sim \zeta^2$ near the surface, superconductivity is killed, where $\zeta = (l_s \xi^2)^{1/3}$ combines the extrapolation length of the surface superconductivity and the coherence length of the bulk superconductivity. We then derive $H_{c2} \sim \Phi_0/\zeta^2 \sim (1 - T/T_c)^{2/3}$, which corresponds to the 6.4 GPa case of Fig. 4b (also see Extended Data Fig. 5).

From the obtained experimental evidence for surface states, we believe the superconducting state of the $\text{Bi}_2\text{Te}_{2.7}\text{Se}_{0.3}$ alloy in Phase I can have nontrivial topology. When the bulk pairing is A_{1g} phase (s -wave), the bulk is fully gapped, surface states form the Fu-Kane model⁵⁶ in 2D, and Majorana zero modes should be found in the vortex cores on the surfaces. When the bulk pairing is A_{1u} phase, the fully-gapped bulk realizes topological superconductivity in class DIII in 3D⁵⁷, and the the surface states are recognized as helical Majorana surface states, which should lead to an asymmetric surface tunneling spectroscopy³¹⁻³³. The bulk pairing symmetry can also

be two-component E_u phase according to recent data, which can spontaneously break in-plane rotation (time-reversal) symmetry and falls into the nematic (chiral) phase. In the nematic phase, topological superconductivity in class DIII is realized in 3D, and the surface states are helical Majorana surface states^{34,35}, where the in-plane critical fields should be anisotropic^{35,46}. While in the chiral phase, bulk superconductivity is nodal with point nodes, and Weyl superconductivity is realized. The surface states are thus Majorana arc states connecting surface-projected Weyl points with opposite Chern numbers⁴². In the chiral phase, time-reversal breaking signals such as Kerr rotation should be observed. These results and discussions above are summarized in Table 1.

The search for topological superconductivity in topological materials such as topological insulators has been longed for in condensed matter physics community during the recent decade. In this work, from carefully designed experiments, and detailed electrical transport, X-ray diffraction, and Raman scattering measurements, we first narrow down the coexisting window of the topological surface states and superconductivity for the same compound. We then apply the detection method proposed recently to measure the critical exponent of critical fields in the temperature dependence, regardless of microscopic details. Finally, we find both the topologically nontrivial and trivial cases for the different superconducting phases predicted by the theory, and hence besides evidence for topological superconductivity, at the same time we also validate this recently proposed method for identifying and distinguishing topological and conventional superconductivity. The current work thus realizes the long-standing dream for the topological superconductivity in most popular topological insulators $\text{Bi}_2\text{Se}_{3-x}\text{Te}_x$ – the alloy compounds of Bi_2Se_3 and Bi_2Te_3 .

1. Kitaev, A. Y. Fault-tolerant quantum computation by anyons. *Ann. Phys.* **303**, 2?30 (2003).
2. Nayak, C., Simon, S. H., Stern, A., Freedman, M. & Sarma, S. D. Non-Abelian anyons and topological quantum computation. *Rev. Mod. Phys.* **80**, 1083-1159 (2008).
3. Kitaev, A. Y. Unpaired Majorana fermions in quantum wires. *Phys.-Usp.* **44**, 131-136 (2001).
4. Read, N. & Green, D. Paired states of fermions in two dimensions with breaking of parity and time-reversal symmetries and the fractional quantum Hall effect. *Phys. Rev. B* **61**, 10267-10297 (2000).
5. Ivanov, D. A. Non-Abelian statistics of half-quantum vortices in p -wave superconductors. *Phys. Rev. Lett.* **86**, 268-271 (2001).
6. Alicea, J., Oreg, Y., Refael, G., von Oppen, F. & Fisher, M. P. A. Non-Abelian statistics and topological quantum information processing in 1D wire networks. *Nat. Phys.* **7**, 412?417 (2011).
7. Thouless, D. J., Kohmoto, M., Nightingale, M. P. & den Nijs, M. Quantized Hall conductance in a two-dimensional periodic potential. *Phys. Rev. Lett.* **49**, 405 (1982).
8. Kane, C. L. & Mele, E. J. Quantum spin Hall effect in graphene. *Phys. Rev. Lett.* **95**, 226801 (2005).
9. Kane, C. L. & Mele, E. J. Z_2 Topological order and the quantum spin Hall effect. *Phys. Rev. Lett.* **95**, 146802 (2005).

10. Fu, L., Kane, C. L. & Mele, E. J. Topological insulators in three dimensions. *Phys. Rev. Lett.* **98**, 106803 (2007).
11. Fu, L. & Kane, C. L. Topological insulators with inversion symmetry. *Phys. Rev. B* **76**, 045302 (2007).
12. Zhang, H., Liu, C.-X., Qi, X.-L., Dai, X., Fang, Z. & Zhang, S.-C. Topological insulators in Bi_2Se_3 , Bi_2Te_3 and Sb_2Te_3 with a single Dirac cone on the surface. *Nature Physics* **5**, 438-442 (2009).
13. Hasan, M. Z. & Kane, C. L. Colloquium: Topological insulators. *Rev. Mod. Phys.* **82**, 3045-3067 (2010).
14. Qi, X. L. & Zhang, S. C. Topological insulators and superconductors. *Rev. Mod. Phys.* **83**, 1057-1110 (2011).
15. Chen, Y. L., Analytis, J. G., Chu, J.-H., Liu, Z. K., Mo, S.-K., Qi, X. L., Zhang, H. J., Lu, D. H., Dai, X., Fang, Z., Zhang, S. C., Fisher, I. R., Hussain, Z. & Shen, Z. X. Experimental realization of a three-dimensional topological insulator, Bi_2Te_3 . *Science* **325**, 178-181 (2009).
16. Xia, Y., Qian, D., Hsieh, D., Wray, L., Pal, A., Lin, H., Bansil, A., Grauer, D., Hor, Y. S., Cava, R. J. & Hasan, M. Z. Observation of a large-gap topological-insulator class with a single Dirac cone on the surface. *Nat. Phys.* **5**, 398-402 (2009).
17. Chen, C. Y., He, S. L., Weng, H. M., Zhang, W. T., Zhao, L., Liu, H. Y., Jia, X. W., Mou, D. X., Liu, S. Y., He, J. F., Peng, Y. Y., Feng, Y., Xie, Z. J., Liu, G. D., Dong, X. L., Zhang, J.,

- Wang, X. Y., Peng, Q. J., Wang, Z. M., Zhang, S. J., Yang, F., Chen, C. T., Xu, Z. Y., Dai, X., Fang, Z. & Zhou, X. J. Robustness of topological order and formation of quantum well states in topological insulators exposed to ambient environment. *Proc. Natl. Acad. Sci. U.S.A.* **109**, 3694-3698 (2012).
18. Qu, D. X., Hor, Y. S., Xiong, J., Cava, R. J. & Ong, N. P. Quantum oscillations and Hall anomaly of surface states in the topological insulator Bi_2Te_3 . *Science* **329**, 821-824 (2010).
19. Ilina, M. A. & Itskevich, E. S. Superconductivity of bismuth telluride. *Sov. Phys. Solid State* **13**, 2098-2100 (1972).
20. Zhang, J. L., Zhang, S. J., Weng, H. M., Zhang, W., Yang, L. X., Liu, Q. Q., Feng, S. M., Wang, X. C., Yu, R. C., Cao, L. Z., Wang, L., Yang, W. G., Liu, H. Z., Zhao, W. Y., Zhang, S. C., Dai, X., Fang, Z. & Jin, C. Q. Pressure-induced superconductivity in topological parent compound Bi_2Te_3 . *Proc. Natl. Acad. Sci. U.S.A.* **108**, 24-28 (2011).
21. Kirshenbaum, K., Syers, P. S., Hope, A. P., Butch, N. P., Jeffries, J. R., Weir, S. T., Hamlin, J. J., Maple, M. B., Vohra, Y. K. & Paglione, J. Pressure-induced unconventional superconducting phase in the topological insulator Bi_2Se_3 . *Phys. Rev. Lett.* **111**, 087001 (2013).
22. Hor, Y. S., Williams, A. J., Checkelsky, J. G., Roushan, P., Seo, J., Xu, Q., Zandbergen, H. W., Yazdani, A., Ong, N. P. & Cava, R. J. Superconductivity in $\text{Cu}_x\text{Bi}_2\text{Se}_3$ and its implication for pairing in the underdoped topological insulator. *Phys. Rev. Lett.* **104**, 057001 (2010).
23. Xu, J. P., Wang, M. X., Liu, Z. L., Ge, J. F., Yang, X. J., Liu, C. H., Xu, Z. A., Guan, D. D., Gao, C. L., Qian, D., Liu, Y., Wang, Q. H., Zhang, F. C., Xue, Q. K. & Jia, J. F. Experimental

- detection of a Majorana mode in the core of a magnetic vortex inside a topological insulator-superconductor $\text{Bi}_2\text{Te}_3/\text{NbSe}_2$ heterostructure. *Phys. Rev. Lett.* **114**, 017001 (2015).
24. He, Q. L., Pan, L., Stern, A. L., Burks, E. C., Che, X. Y., Yin, G., Wang, J., Lian, B., Zhou, Q., Choi, E. S., Murata, K., Kou, X. F., Chen, Z. J., Nie, T. X., Shao, Q. M., Fan, Y. B., Zhang, S. C., Liu, K., Xia, J. & Wang, K. L. Chiral Majorana fermion modes in a quantum anomalous Hall insulator-superconductor structure. *Science* **337**, 294-299 (2017).
25. Wray, L. A., Xu, S. Y., Xia, Y. Q., Qian, D., Fedorov, A. V., Lin, H., Bansil, A., Hor, Y. S., Cava, R. J. & Hasan, M. Z. Observation of topological order in a superconducting doped topological insulator. *Nat. Phys.* **6**, 855-859 (2010).
26. Kriener, M., Segawa, K., Ren, Z., Sasaki, S. & Ando, Y. Bulk superconducting phase with a full energy gap in the doped topological insulator $\text{Cu}_x\text{Bi}_2\text{Se}_3$. *Phys. Rev. Lett.* **106**, 127004 (2011).
27. Levy, N., Zhang, T., Ha, J., Sharifi, F., Talin, A. A., Kuk, Y. & Stroscio, J. A. Experimental evidence for *s*-wave pairing symmetry in superconducting $\text{Cu}_x\text{Bi}_2\text{Se}_3$ single crystals using a scanning tunneling microscope. *Phys. Rev. Lett.* **110**, 117001 (2013).
28. Matano, K., Kriener, M., Segawa, K., Ando, Y. & Zheng, G. Q. Spin-rotation symmetry breaking in the superconducting state of $\text{Cu}_x\text{Bi}_2\text{Se}_3$. *Nat. Phys.* **12**, 852-854 (2016).
29. Yonezawa, S., Tajiri, K., Nakata, S., Nagai, Y., Wang, Z. W., Segawa, K., Ando, Y. & Maeno, Y. Thermodynamic evidence for nematic superconductivity in $\text{Cu}_x\text{Bi}_2\text{Se}_3$. *Nat. Phys.* **13**, 123-126 (2017).

30. Peng, H. B., De, D., Lv, B., Wei, F. Y. & Chu, C. W. Absence of zero-energy surface bound states in $\text{Cu}_x\text{Bi}_2\text{Se}_3$ studied via Andreev reflection spectroscopy. *Phys. Rev. B* **88**, 024515 (2013).
31. Fu, L. & Berg, E. Odd-parity topological superconductors: theory and application to $\text{Cu}_x\text{Bi}_2\text{Se}_3$. *Phys. Rev. Lett.* **105**, 097001 (2010).
32. Hao, L. & Lee, T. K. Surface spectral function in the superconducting state of a topological insulator. *Phys. Rev. B* **83**, 134516 (2011).
33. Hsieh, T. H. & Fu, L. Majorana fermions and exotic surface Andreev bound states in topological superconductors: Application to $\text{Cu}_x\text{Bi}_2\text{Se}_3$. *Phys. Rev. Lett.* **108**, 107005 (2012).
34. Fu, L. Odd-parity topological superconductor with nematic order: application to $\text{Cu}_x\text{Bi}_2\text{Se}_3$. *Phys. Rev. B* **90**, 100509(R) (2014).
35. Venderbos, J. W. F., Kozii, V. & Fu, L. Identification of nematic superconductivity from the upper critical field. *Phys. Rev. B* **94**, 094522 (2016).
36. Liu, Z. *et al.* Superconductivity with topological surface state in $\text{Sr}_x\text{Bi}_2\text{Se}_3$. *J. Am. Chem. Soc.* **137**, 10512-10515 (2015).
37. Shruti, V. K., Maurya, P., Neha, P., Srivastava, P. & Patnaik, S. Superconductivity by Sr intercalation in the layered topological insulator Bi_2Se_3 . *Phys. Rev. B* **92**, 020506(R) (2015).
38. Pan, Y. *et al.* Rotational symmetry breaking in the topological superconductor $\text{Sr}_x\text{Bi}_2\text{Se}_3$ probed by upper-critical field experiments. *Sci. Rep.* **6**, 28632 (2016).

39. Du, G., Li, Y.-F., Schneeloch, J., Zhong, R. D., Gu, G.-D., Yang, H., Lin, H. & Wen, H.-H. Superconductivity with two-fold symmetry in topological superconductor $\text{Sr}_x\text{Bi}_2\text{Se}_3$. *Sci. China Phys. Mech. Astron.* **60**, 037411 (2017).
40. Qiu, Y., Sanders, K. N., Dai, J., Medvedeva, J. E., Wu, W., Ghaemi, P., Vojta, T. & Hor, Y. S. Time reversal symmetry breaking superconductivity in topological materials. arXiv:1512.03519 (2015).
41. Asaba, T. *et al.* Rotational symmetry breaking in a trigonal superconductor Nb-doped Bi_2Se_3 . *Phys. Rev. X* **7**, 011009 (2017).
42. Yuan, N. F. Q., He, W.-Y. & Law, K. T. Superconductivity-induced ferromagnetism and Weyl superconductivity in Nb-doped Bi_2Se_3 . *Phys. Rev. B* **95**, 201109(R) (2017).
43. Smylie, M. P. *et al.* Evidence of nodes in the order parameter of the superconducting doped topological insulator $\text{Nb}_x\text{Bi}_2\text{Se}_3$ via penetration depth measurements. *Phys. Rev. B* **94**, 180510(R) (2016).
44. Smylie, M. P. *et al.* Robust odd-parity superconductivity in the doped topological insulator $\text{Nb}_x\text{Bi}_2\text{Se}_3$. *Phys. Rev. B* **96**, 115145 (2017).
45. Kurter, C. *et al.* Conductance spectroscopy of exfoliated thin flakes of $\text{Nb}_x\text{Bi}_2\text{Se}_3$. *Nano Lett.* **19**, 38745 (2019).
46. Shen, J. *et al.* Nematic topological superconducting phase in Nb-doped Bi_2Se_3 . *npj Quantum Mater.* **2**, 59 (2017).

47. Fu, L. Topological crystalline insulators. *Phys. Rev. Lett.* **106**, 106802 (2011).
48. Fang, C., Fu, L. New classes of three-dimensional topological crystalline insulators: Non-symmorphic and magnetic. *Phys. Rev. B* **91**, 161105 (2015).
49. Fang, C., Fu, L. New classes of topological crystalline insulators having surface rotation anomaly. *Sci. Adv.* **20**, eaat2374 (2019).
50. Zhu, L., Wang, H., Wang, Y. C., Lv, J., Ma, Y. M., Cui, Q. L., Ma, Y. M. & Zou, G. T. Substitutional alloy of Bi and Te at high pressure. *Phys. Rev. Lett.* **106**, 145501 (2010).
51. Vilaplana, R., Santamaria-Perez, D., Gomis, O., Manjon, F. J., Gonzalez, J., Segura, A., Munoz, A., Rodriguez-Hernandez, P., Perez-Gonzalez, E., Marin-Borras, V., Munoz-Sanjose, V., Drasar, C. & Kucek, V. Structural and vibrational study of Bi_2Se_3 under high pressure. *Phys. Rev. B* **84**, 184110 (2011).
52. Nakayama, A., Einaga, M., Tanabe, Y., Nakano, S., Ishikawa, F. & Yamada, Y. Structural phase transition in Bi_2Te_3 under high pressure. *High Pressure Res.* **29**, 245-249 (2009).
53. Korobeinikov, I. V., Luk'yanova, L. N., Vorontsov, G. V., Shchennikov, V. V. & Kutasov, V. A. Thermoelectric properties of $n\text{-Bi}_2\text{Te}_{3-x-y}\text{Se}_x\text{S}_y$ solid solutions under high pressure. *Phys. Solid State* **56**, 263-269 (2014).
54. Richter, W., Köhler, H. & Becker, C. R. A Raman and far-infrared investigation of phonons in the rhombohedral $\text{V}_2\text{-VI}_3$ compounds Bi_2Te_3 , Bi_2Se_3 , Sb_2Te_3 and $\text{Bi}_2(\text{Te}_{1-x}\text{Se}_x)_3$ ($0 < x < 1$), $(\text{Bi}_{1-y}\text{Sb}_y)_2\text{Te}_3$ ($0 < y < 1$). *Phys. Status Solidi B* **84**, 619-628 (1977).

55. Yuan, N. F. Q. & Chen, X. J. Critical field measure for topological superconductivity in a superconductor with surface or edge states (2022).
56. Fu, L. & Kane, C. L. Superconducting proximity effect and Majorana fermions at the surface of a topological insulator. *Phys. Rev. Lett.* **100**, 096407 (2008).
57. Chiu, C.-K., Teo, Jeffrey C. Y., Schnyder, A. P. & Ryu, S. Classification of topological quantum matter with symmetries. *Rev. Mod. Phys.* **88**, 035005 (2016).

Acknowledgements This work was funded through the Shenzhen Science and Technology Program (Grant No. KQTD20200820113045081), the Basic Research Program of Shenzhen (Grant No. JCYJ20200109112810241), and the National Key R&D Program of China (Grant No. 2018YFA0305900). N.F.Q.Y. acknowledges the National Natural Science Foundation of China (Grant. No. 12174021) for the financial support. The sample preparation in CAS was supported by National Natural Science Foundation of China under Grant Nos. 51672278, 11674322, and 11374306. The synchrotron X-ray diffraction measurements were performed at GeoSoilEnviroCARS (The University of Chicago, Sector 13), Advanced Photon Source (APS), Argonne National Laboratory. GeoSoilEnviroCARS is supported by the National Science Foundation–Earth Sciences (EAR–1634415) and Department of Energy- GeoSciences (DE-FG02-94ER14466). The research used resources of the Advanced Photon Source, a U.S. Department of Energy (DOE) Office of Science User Facility operated for the DOE Office of Science by Argonne National Laboratory under Contract No. DE-AC02-06CH11357.

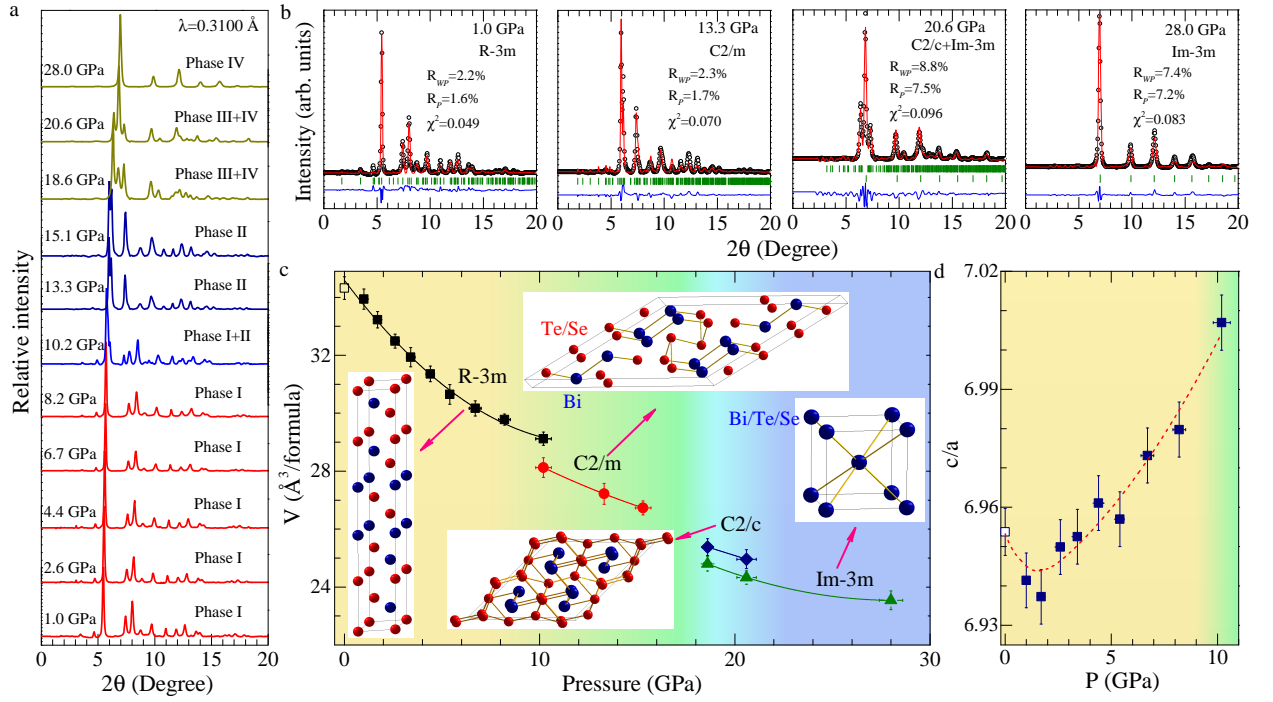


Figure 1 | High-pressure structures of $\text{Bi}_2\text{Te}_{2.7}\text{Se}_{0.3}$ at room temperature. **a**, Synchrotron X-ray diffraction patterns at various pressures up to 28.0 GPa with the radiation wavelength of 0.3100 \AA . **b**, Rietveld refinement results at pressure of 1.0, 13.3, 20.6, and 28.0 GPa for representative phase with space group of $R-3m$ (Phase I), $C2/m$ (Phase II), $C2/c$ (Phase III), and $Im-3m$ (Phase IV), respectively. The open circles are the measured data points. The curves are the refinement results. Their difference profiles are shown at the bottoms. The positions of the Bragg reflections are marked by the vertical lines for each phase. The agreement between the experiments and structure models is evaluated by the residual parameters $R_{wp}=2.2\%$, $R_p=1.6\%$, and $\chi^2=0.049$ for pressure of 1.0 GPa; $R_{wp}=2.3\%$, $R_p=1.7\%$, and $\chi^2=0.070$ for pressure of 13.3 GPa; $R_{wp}=8.8\%$, $R_p=7.5\%$, and $\chi^2=0.096$ for pressure of 20.6 GPa; and $R_{wp}=7.4\%$, $R_p=7.2\%$, and $\chi^2=0.083$ for pressure of 28.0 GPa, respectively. **c**,

Evolution of the volume per formula of each phase with pressure. The atomic arrangement in a unit cell is shown for the corresponding phase pointed by arrow. The atoms of Bi and Te/Se are drawn in two different balls with different colours for the first three phases. These atoms share the same positions in Phase IV with the space group of $Im-3m$. **d**, Pressure dependence of the axial ratio c/a in Phase I with the space group of $R-3m$. The dashed line is drawn for the guide of the eye. There is a minimum at a pressure close to 2 GPa. The open squares in **c** and **d** are the data points at ambient pressure.

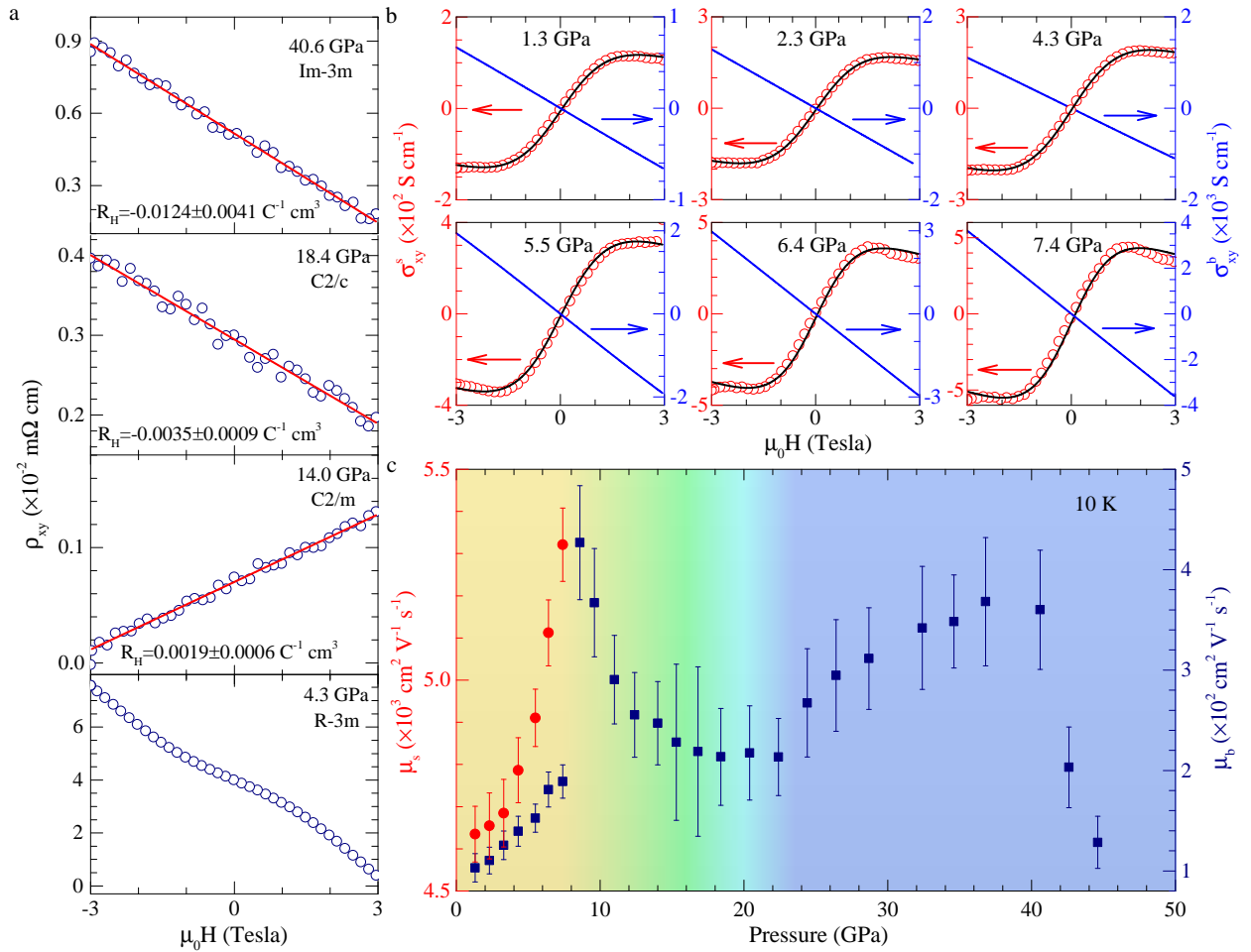


Figure 2 | High-pressure Hall effect of $\text{Bi}_2\text{Te}_{2.7}\text{Se}_{0.3}$ at temperature of 10 K. **a**, Representative Hall resistivity ρ_{xy} vs magnetic fields up to ± 3 Tesla for each phase from the bottom to top with the space group of $R-3m$, $C2/m$, $C2/c$, and $Im-3m$ at pressure of 4.3 , 14.0, 18.4, and 40.6 GPa, respectively. The data points are denoted by the open cycles. The lines are the the fitting results to the experiments. The nonlinear profile of the Hall resistivity in Phase I at pressure of 4.3 GPa is a result of the combination from the contributions of the bulk and surface states. **b**, Separation of the bulk and surface contributions to the Hall conductivity in Phase I with the space group of $R-3m$ for selected pressures. The surface Hall

conductivity σ_{xy}^s is obtained by subtracting the bulk component σ_{xy}^b from the observed Hall conductivity σ_{xy} . **c**, Pressure dependence of the mobility in the surface (μ_s) and bulk (μ_b) states in Phase I with the space group of $R\bar{3}m$ and the bulk mobility in the followed phases at higher pressures.

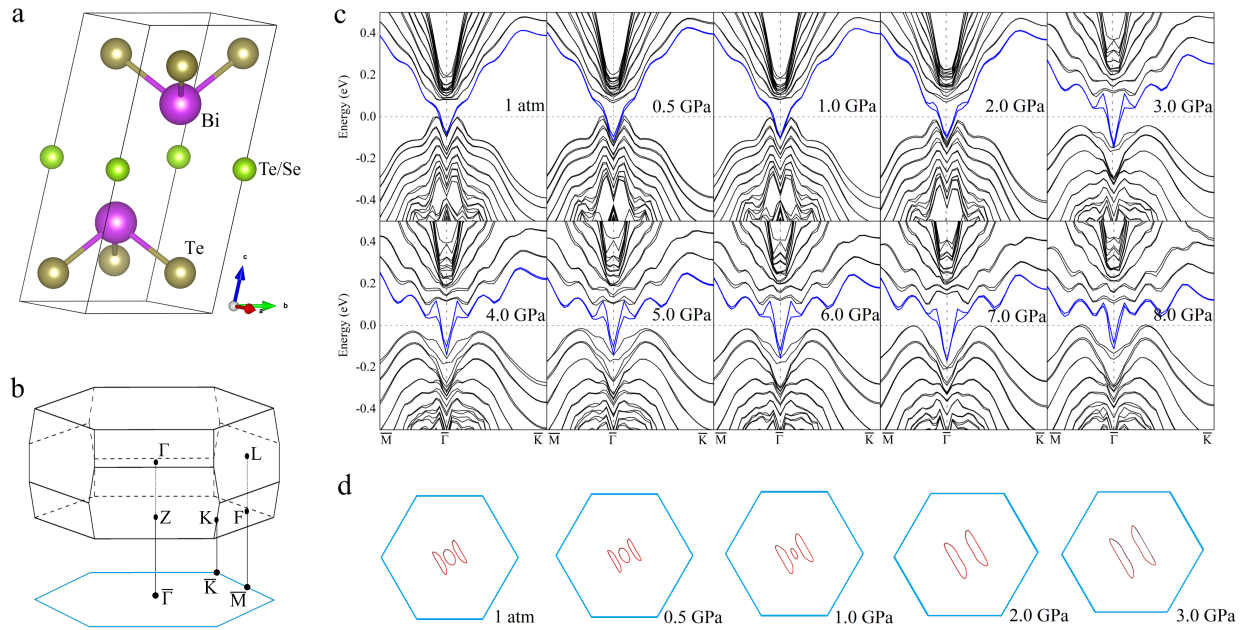


Figure 3 | Electronic structures of $\text{Bi}_2\text{Te}_{2.7}\text{Se}_{0.3}$ in the $R\text{-}3m$ phase at high pressures. **a, A unit cell with the space group of $R\text{-}3m$. **b**, The first Brillouin zone of the alloy with high symmetry points (upper panel) and the two-dimensional projection along the (001) surface (lower panel). **c**, The slab band structures at various pressures up to 8.0 GPa. The blue curves represent the metallic surface bands and the black ones are the bulk electronic structures. **d**, The evolution of energy contours of the top bulk valence band with pressure. As pressure increases, the number of distinct energy contours changes from 3 to 2, indicating the electronic topological transition around 2 GPa.**

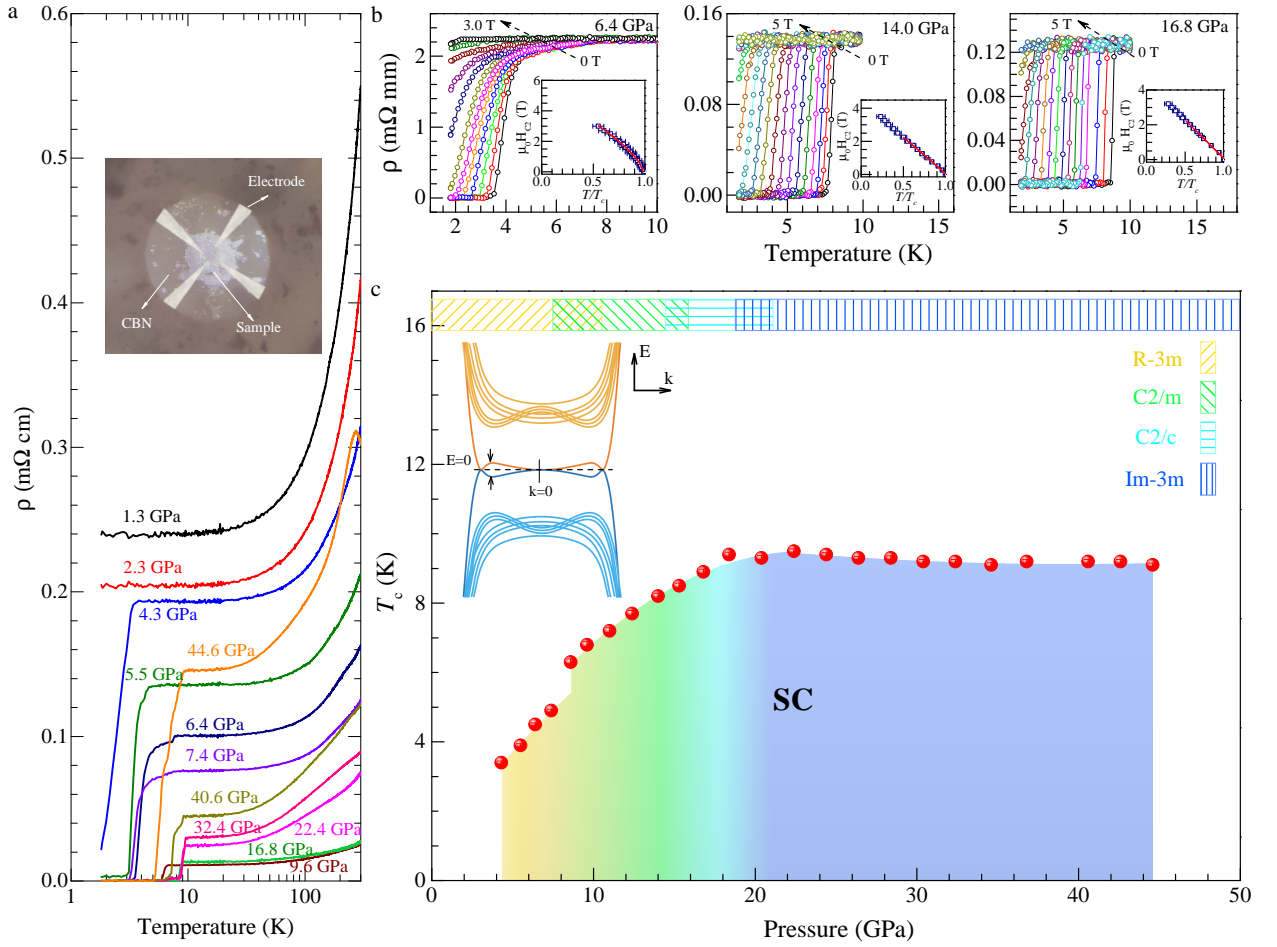


Figure 4 | Temperature-pressure phase diagram of $\text{Bi}_2\text{Te}_{2.7}\text{Se}_{0.3}$. **a**, Temperature dependence of the resistivity ρ for selected pressures up to 40.6 GPa. The ρ drop appears at 4.3 GPa and down to zero to low temperatures at higher pressures. Inset: Photograph for the sample attached by four electrodes in the chamber made by cubic boron nitride. **b**, Temperature-dependent resistivity curve with the applied magnetic fields at pressure of 6.4, 14.0, and 16.8 GPa, respectively. Insets: The upper critical field as a function of the reduced temperature (T/T_c) with T_c being the superconducting transition temperature for representative pressures in different phases. The zero-field T_c value for pressure of 6.4, 14.0, and 16.8 GPa

is 4.50(4), 8.21(8), and 8.92(8) K, respectively. T_c is chosen as the onset temperature of superconductivity to avoid the influence of possible superconducting vortex phases. The fitting to the experimental data points near T_c in the T/T_c range of 0.5 to 1 in the curve by using $\mu_0 H_{c2} \sim (1 - T/T_c)^\alpha$ with α being 2/3 for pressure of 6.4 GPa and 1.0 for pressure of 14.0 and 16.8 GPa, respectively. **c**, Pressure dependence of T_c crossing different phases. The phase region is indicated by the different type of mark. The phases and their boundaries are determined from the results of the X-ray diffraction, Raman scattering, and Hall effect measurements. Errors are smaller than the size of the data points.

Table 1 | Possibilities of topological superconductivity. Corresponding to the bulk pairing symmetry, the pairing topology is listed in the bulk and on the surface.

Symmetry	Bulk	Surface
A_{1g}	Trivial, fully gapped	Fu-Kane model
A_{1u}	DIII in 3D, fully gapped	Helical Majorana surface states
E_u nematic	DIII in 3D, fully gapped	Helical Majorana surface states
E_u chiral	Weyl superconductor, point nodes	Chiral Majorana arc states

METHODS:

Sample synthesis. Alloyed powders of $\text{Bi}_2\text{Te}_{2.7}\text{Se}_{0.3}$ were synthesized according to the stoichiometry with appropriate amounts of element Bi (99.999%), Te (99.999%), and Se (99.999%) purchased from Alfa Aesar. The powder mixture was loaded into quartz ampoule and sealed under vacuum at 10^{-3} Pa, and then heated at 1123 K for 24 hours. The obtained ingot was then ground using a mortar type grinder for 30 minutes with a speed of 125 rpm. The obtained powders were compacted with tungsten carbide mould by hot-pressing at 633 K at pressure of 300 MPa in vacuum for one hour. Consequently, disk-shaped bulk samples with 2 mm in height and 13 mm in diameter were obtained. The specimens for transport, structure, and spectroscopy measurements under pressure were cut from the as-prepared bulk samples. The synthesized samples are the *n*-type.

High-pressure X-ray diffraction measurements. The ambient-pressure structure of the sample was investigated by using a RigakuD/MAX-2550PC diffractometer with $\text{Cu-K}\alpha$ radiation in wavelength of 1.5406 Å. For the high-pressure structural study, synchrotron X-ray diffraction (XRD) patterns were collected at GeoSoilEnviroCARS (Sector 13), Advanced Photon Source, Argonne National Laboratory, USA. The wavelength of 0.3100 Å and the size of the focus beam of less than 2 μm were chosen for the measurements. The sample was pressed into powders before being placed into the chamber. Neon was loaded as the transmitting medium. The obtained two-dimensional XRD patterns were integrated into one-dimensional patterns with the help of the Fit2D software⁵⁸. The integrated intensity vs 2θ diffraction patterns were analyzed through the Rietveld method using the GSAS

package⁵⁹. The pressure was calibrated by using the ruby fluorescence shift⁶⁰ and implemented at room temperature. The collected room-temperature XRD patterns for selected pressures are shown in Fig. 1a. The refinements to the obtained data for four representative phases with different structure symmetries are shown in Fig. 1b. The details of the refinement results for these selected pressures are summarized in Extended Data Table 1. The evolution of the obtained volume per formula at each phase with pressure is presented in Fig. 1c. The pressure dependence of the obtained axial ratio of c/a for the first phase is plotted in Fig. 1d.

High-pressure Raman scattering measurements. Raman spectra were measured using a single-stage spectrograph equipped with a thermoelectrically cooled charge-coupled device. The Raman notch filters were of a very narrow bandpass, allowing Raman measurements down to 10 cm^{-1} in the stokes and anti-stokes. The 488 nm excitation incidents were used to illuminate an approximately $5\times 5\text{ }\mu\text{m}^2$ spot on the surface of the sample. The excitation strength was monitored by using a power meter. The power of 1.5 mW (0.5 mW) was chosen for the measurements at room temperature (low temperatures). In both measurements, neon was loaded as a transmitting medium. The pressure was gauged by the the ruby fluorescence shift⁶⁰. The results for the room temperature and low temperatures are shown in Extended Data Figs. 1, 4, and 6, respectively.

High-pressure resistivity and Hall effect measurements. For the high-pressure resistivity and Hall effect measurements, a nonmagnetic diamond anvil cell made of Cu-Be alloy was used for Physical Properties Measurements System from U.S. Quantum Design⁶¹. This customized cell has two symmetrical diamond anvils and the diameter of the anvil culets is 300

μm . A steel flake was used as the gasket with the sample chamber of $150\ \mu\text{m}$ diameter. The gasket was insulated with cubic boron nitride and silver epoxy. A cut piece of the polycrystalline sample was placed into the sample chamber. Four Pt wires were placed on the surface of one side of the insulated gasket with the linkage of the sample and the external Cu wires. A standard four-probe method was used for the electrical transport measurements. The resistivity and Hall coefficient were determined in terms of the van der Pauw method⁶². For this method, the thickness of the measured sample is the only needed dimensional parameter. The sample thickness for the electrical transport measurements is $32\ \mu\text{m}$. No pressure transmitting medium was used for such electrical transport measurements. The loaded ruby chip was used to determine pressure. The Hall effect measurements were taken at low temperature of 10 K. The results are shown in Fig. 2. The Hall conductivity σ_{xy} and the contributions from the bulk and surface states for pressures of interest in Phase I are shown in Fig. 2b and Extended Data Figs. 2 and 3, respectively. The temperature-dependent resistivities at selected pressures up to 40.6 GPa are shown in Figs. 4a and 4b.

Structural evolution with pressure. Our experiments support the following structural evolution path of $\text{Bi}_2\text{Te}_{2.7}\text{Se}_{0.3}$ with pressure: from its initial rhombohedra structure (Phase I) with the space group of $R\bar{3}m$ to the final disordered body-centered cubic structure (Phase IV) with the space group of $Im\bar{3}m$ after passing two intermediate monoclinic phases with the space group of $C2/m$ for Phase II and $C2/c$ for Phase III. We observed the anomaly of the axial ratio c/a in Phase I with the minimum at a pressure close to 2 GPa. This phenomenon was also observed in the other studies on the similar compounds Bi_2Te_3 ^{52,63,64} and

Bi_2Se_3 ^{51,64}. The obtained structural evolution path with pressure for $\text{Bi}_2\text{Te}_{2.7}\text{Se}_{0.3}$ is in good agreement with the observations for the similar systems such as Bi_2Te_3 ^{50,52}, Bi_2Se_3 ⁵¹, and Sb_2Te_3 ⁶⁵.

Assignment of the phonon modes. There are four phases at high pressures from the structural study. Phonon modes can be observed at low pressures but become invisible at high pressure (Extended Data Figs. 1 and 4). The spectra change profiles at the boundary for a certain pressure where the phase transition takes place. The critical pressures for the profile changes from the Raman spectra are consistent with those for the phase transformation detected from the XRD measurements (Fig. 1).

The initial phase (I) of $\text{Bi}_2\text{Te}_{2.7}\text{Se}_{0.3}$ has the rhombohedra structure with the space group of $R\bar{3}m$. Group theory predicts 10 zone-center modes with the irreducible representations: $\Gamma_I = 2A_{1g} + 3A_{2u} + 2E_g + 3E_u$. Here A_{2u} and E_u are two acoustic branches, and A_{1g} and E_g are from optical branches. Only two A_{1g} modes and two E_g modes are Raman active.

The first intermediate phase (II) of $\text{Bi}_2\text{Te}_{2.7}\text{Se}_{0.3}$ possesses the monoclinic structure with the space group of $C2/m$. There are 30 vibrational modes from the group theory prediction with the representation: $\Gamma_{II} = 10A_g + 10B_u + 5A_u + 5B_g$. Among them, the A_u and B_u are from the acoustic branches and the rest are optical phonons. Therefore, 10 A_g and 5 B_g modes are Raman active.

The second intermediate phase (III) of $\text{Bi}_2\text{Te}_{2.7}\text{Se}_{0.3}$ adopts the monoclinic structure with the space group of $C2/c$. Group theoretical considerations predict 30 vibrational modes

with the following representation form: $\Gamma_{III} = 7A_g + 7A_u + 8B_g + 8B_u$. Here the A_u and B_u modes are from the acoustic branches and the A_g and B_g modes are from the optical branches. Thus, 15 zone-center Raman active modes ($7A_g+8B_g$) are expected to be observed for this phase.

The last phase (IV) of $\text{Bi}_2\text{Te}_{2.7}\text{Se}_{0.3}$ has the disordered body-centered cubic structure with the space group of $Im-3m$. No Raman active modes are expected for this symmetry.

Our in-house built Raman system captures almost all these assigned features. For example, we observed the four Raman active modes for Phase I over the whole pressure range at both the room temperature (Extended Data Fig. 1) and low temperatures down to 3.6 K (Extended Data Figs. 4 and 6). The featureless background in Phase IV was also observed in both cases. The rather rich features below the wavenumber of 50 cm^{-1} in the two intermediate phases were found from the current study. The phonon peaks and profiles above 50 cm^{-1} for these two phases are similar to the observations for Bi_2Se_3 ⁵¹.

We observed four Raman-active modes ($2A_{1g}+2E_g$) in the studied $\text{Bi}_2\text{Te}_{2.7}\text{Se}_{0.3}$ in the wavenumbers down to 10 cm^{-1} for Phase I. At both room temperature and low temperature, the frequencies of all these phonon modes change slope at around 2 GPa when increasing with pressure. Interestingly, the FWHM changes with pressure in different manners for the A_{1g} and E_g mode. The two E_g modes correspond to atomic vibrations in the plane of the layers, while the A_{1g} modes correspond to vibrations along the c axis perpendicular to the layers⁵⁴. Upon compression, the FWHM has the maximum (minimum) for the E_g^1 (E_g^2) mode at a pressure close to 2 GPa. For the two A_{1g} modes, their FWHM just changes slope when

narrowing down with increasing pressure. These results are summarized in Extended Data Figs. 1, 4, and 6. The non-monotonic pressure dependences were also observed in the sister systems Bi_2Te_3 ^{51,64}, Bi_2Se_3 ^{51,64}, and Sb_2Se_3 ⁶⁶.

Determination of the mobility and concentration of the charge carriers. The high-pressure Hall effect measurements were used to determine the Hall resistivity or conductivity along the xx and xy directions. The components for the Hall resistivity and conductivity along the xx and xy directions are related to the two expressions $\sigma_{xx} = 1/\rho_{xx}$ and $\sigma_{xy} = \rho_{xy}/(\rho_{xx}^2 + \rho_{xy}^2)$.

The Hall coefficient R_H is thus determined by fitting the obtained Hall resistivity ρ_{xy} along the xy direction vs magnetic field curve for the bulk material on the assumption that the electrical transport is dominated by free electrons. The carrier concentration n_H can be obtained by using the formula $n_H = 1/(eR_H)$ with e being the electron charge. The Hall mobility (μ) can be calculated based on the relation $\mu = \sigma_{xx}R_H$ if the electrical conductivity σ_{xx} is known. In the absence of the topological order, the Hall resistivity varies with the low magnetic field in a linear manner if the carrier is the single type. These conditions are fully satisfied for the high-pressure phases with the space group of $C2/m$, $C2/c$, and $Im-3m$ (Fig. 2a). We thus can determine the bulk mobility μ_b of this material at each pressure of the corresponding phase. The μ_b values at selected pressures are shown in Fig. 2c.

For the topological insulating state, the Hall resistivity does not exhibit a linear behaviour but has a resonant structure in weak magnetic field (Fig. 2a and Extended Data Fig. 2). The observed Hall conductivity σ_{xy} can be described as the sum of the surface Hall con-

ductivity σ_{xy}^s and the bulk σ_{xy}^b ¹⁸:

$$\sigma_{xy} = \sigma_{xy}^s + \sigma_{xy}^b . \quad (1)$$

The surface conductivity σ_{xy}^s can be expressed as:

$$\sigma_{xy}^s = \frac{2\pi e^3}{dh^2} \frac{Bl^2}{1 + (\mu_s B)^2} , \quad (2)$$

where d is the sample thickness, l is the mean free path, and μ_s is the surface carrier mobility.

The bulk conductivity σ_{xy}^b can be expressed by the semiclassical form:

$$\sigma_{xy}^b = n_{eff} e \mu_b \frac{\mu_b B}{1 + (\mu_b B)^2} , \quad (3)$$

where n_{eff} is the effective carrier concentration and μ_b is the bulk carrier mobility.

Equations (1)-(3) can be used to fit the σ_{xy} vs H curve once the sample thickness d is known. The fitting gives the values of μ_s for the surface and μ_b and n_{eff} for the bulk along with l at each pressure. The fitting is in good agreement with the observed σ_{xy} curve (Extended Data Fig. 2). The decomposition of σ_{xy} into the surface and bulk term is presented in Fig. 2b. The obtained mobility of the two components as a function of pressure is plotted in Fig. 2c. The results for the n_{eff} and l for the bulk state in Phase I together with the bulk carrier concentration n_H in the other phases are summarized in Extended Data Fig. 3.

Pressure-induced electronic topological transition. The anomalies were observed in the studied $\text{Bi}_2\text{Te}_{2.7}\text{Se}_{0.3}$ from pressure dependences of the axial ratio c/a (Fig. 1d) and phonon modes (Extended Data Figs. 1c and 1d, 4b and 4c) in Phase I. The similar behaviours were also observed in the other $\text{V}_2\text{-VI}_3$ compounds with topological insulating states^{51,52,63,64,66}.

These anomalies take place within the same structure of Phase I. These are not a result of structural transition but may be considered as experimental evidence for the possible electronic topological transition (ETT) in these compounds at their initial phase. Pressure-driven ETT was confirmed in Bi_2Te_3 through the measurements of the Shubnikov-de Haas oscillations⁶⁷.

Seebeck coefficient measurements were recognized as an effective, sensitive, and powerful tool for detecting the ETT^{68,69}. In the vicinity of the ETT, the Seebeck coefficient should exhibit an asymmetric shape⁷⁰. The anomaly in the pressure-dependent Seebeck coefficient in Bi_2Te_3 ⁷¹ was reported at the same critical point for the ETT indicated by the Shubnikov-de Haas effect⁶⁷. This demonstrates that the Seebeck coefficient measurements are a rather reliable means to study the ETT phenomenon. Meanwhile, the electrical resistivity also shows a sudden change at such a transition⁷⁰. Such behaviours were indeed observed from the experiments^{53,72-75}. All these experiments along with our measurements support pressure-induced ETT in the $\text{V}_2\text{-VI}_3$ compounds in Phase I.

For $\text{Bi}_2\text{Te}_{2.7}\text{Se}_{0.3}$ with n -type carriers, we observed a minimum of the c/a ratio (Fig. 1d), anomalies of the phonon modes (Extended Data Figs. 1 and 4), abrupt change of the bulk mobility (Fig. 3c), maximum of the effective carrier concentration (Extended Data Fig. 3) at pressure around 2 GPa. For this compound, the Seebeck coefficient, resistivity, and thus power factor, mobility and its product with the effective mass also exhibited anomalies at the same pressure⁵³. Our calculated results shown in Fig. 3d clearly reveal pressure-induced ETT. All these results can be explained by the existence of the ETT at pressure of 2 GPa in

the studied compound.

Comparison of superconducting phases in $\text{Bi}_2\text{Te}_{2.7}\text{Se}_{0.3}$ with Bi_2Te_3 and Bi_2Se_3 . We have demonstrated that the nontrivial topological state of $\text{Bi}_2\text{Te}_{2.7}\text{Se}_{0.3}$ only exists in Phase I from Hall effect measurements (Fig. 2). Thus, topological superconductivity is only expected in Phase I with the space group of $R-3m$. The topological orders are absent in the rest phases with the space group of $C2/m$, $C12c$, and $Im-3m$.

Now let us compare our findings in $\text{Bi}_2\text{Te}_{2.7}\text{Se}_{0.3}$ with the experiments for the two ending compounds Bi_2Te_3 and Bi_2Se_3 in the literature.

For Bi_2Se_3 , superconductivity was reported to start from Phase II after undertaking the first structure transition from $R-3m$ to $C2/m$ ^{21,76}. Since the topological orders are absent in the last three high-pressure phases, the experiments do not support the existence of topological superconductivity in Bi_2Se_3 at high pressures.

For Bi_2Te_3 , the experiments delivered rather rich information. An early study¹⁹ in 1972 revealed that superconductivity occurs in both p and n -type Bi_2Te_3 at pressure near 6 GPa. These findings were later confirmed by many groups after the birth of the topological insulating states in this system. Specifically, two groups^{20,77} reported the occurrence of superconductivity at pressure as low as 3 GPa in p -type Bi_2Te_3 single crystal with $c\text{BN}$ and NaCl as pressure-transmitting medium, respectively. These observations suggested the possible coexistence of superconductivity with the topological order in Phase I of p -type Bi_2Te_3 . A combined electrical transport and XRD study⁷⁸ on p -type Bi_2Te_3 revealed that superconductivity takes place for all four phases and can appear in the initial phase. It would

be ideal if the experimental evidence for the nontrivial topological order had been provided from their experiments. Meanwhile, superconductivity was observed at pressure of 11 GPa in powder sample with the mixture of Fluorinert FC-77 and FC-70 (1:1 in volume) as a pressure-transmitting medium⁷⁵ and near 7 GPa in single crystal with glycerol as a medium⁷⁹. Although the structure measurements on these samples were not carried out, these authors thought that superconductivity occurs in their samples in Phase II when the structural transition takes place from $R-3m$ to $C2/m$.

First-principles calculations. In order to calculate the surface electronic structure, the primitive cell of Bi_2Te_3 parent compound is chosen as shown in Fig. 3a. The (001) surface has been proved to have metallic surface states in early calculations⁸⁰. We first prepared (001)-oriented 10-monolayers-thick crystal slabs of Bi_2Te_3 with experimental lattice parameters, then three Te atoms at one Te position are replaced by Se atom to make an alloy. The vacuum layer was 15 Å thick to ensure decoupling between neighbouring slabs. The first Brillouin zone for Bi_2Te_3 and the two-dimensional Brillouin Zone of the (001) projected surface are shown in Fig. 3b. The slab band structures at different pressures are given in Fig. 3c. The isoenergetic surfaces close to the top of the valence bands for the selected pressures are shown in Fig. 3d. In all these calculations, the experimentally obtained equation of states for $\text{Bi}_2\text{Te}_{2.7}\text{Se}_{0.3}$ was used (Fig. 1c).

We performed all the first-principles calculations in the framework of the density functional theory^{81,82}, as implemented in the Vienna *ab initio* simulation package⁸³⁻⁸⁵. For self-consistent field calculations, we used the Perdew-Burke-Ernzerhof type generalized gradient

approximation⁸⁶ by setting the plane-wave basis expansion as 500 eV with a **k**-point grid taken as $8 \times 8 \times 4$. The spin-orbit coupling was considered during the calculations.

58. Hammersley, A. P., Svensson, S. O., Hanfland, M., Fitch, A. N. & Hausermann, D. Two-dimensional detector software: From real detector to idealised image or two-theta scan. *High Press. Res.* **14**, 235-248 (1996).
59. Toby, B. H. EXPGUI, a graphical user interface for GSAS. *J. Appl. Cryst.* **34**, 210-213 (2001).
60. Mao, H. K., Bell, P. M., Shaner, J. W. & Stembey, D. J. Specific volume measurements of Cu, Mo, Pd, and Ag and calibration of the ruby R_1 fluorescence pressure gauge from 0.06 to 1 Mbar. *J. Appl. Phys.* **49**, 3276-3283 (1978).
61. Gavriluk, A. G., Mironovich, A. A. & Struzhkin, V. V. Miniature diamond anvil cell for broad range of high pressure measurements. *Rev. Sci. Instrum.* **80**, 043906 (2009).
62. Van der Pauw, L. J. A method of measuring specific resistivity and Hall effect of discs of arbitrary shape. *Philips Res. Repts.* **13**, 1-9 (1958).
63. Polian, A., Gauthier, M., Souza, S. M., Triches, D. M., Cardoso de Lima, J. & Grandi, T. A. Two-dimensional pressure-induced electronic topological transition in Bi_2Te_3 . *Phys. Rev. B* **83**, 113106 (2011).

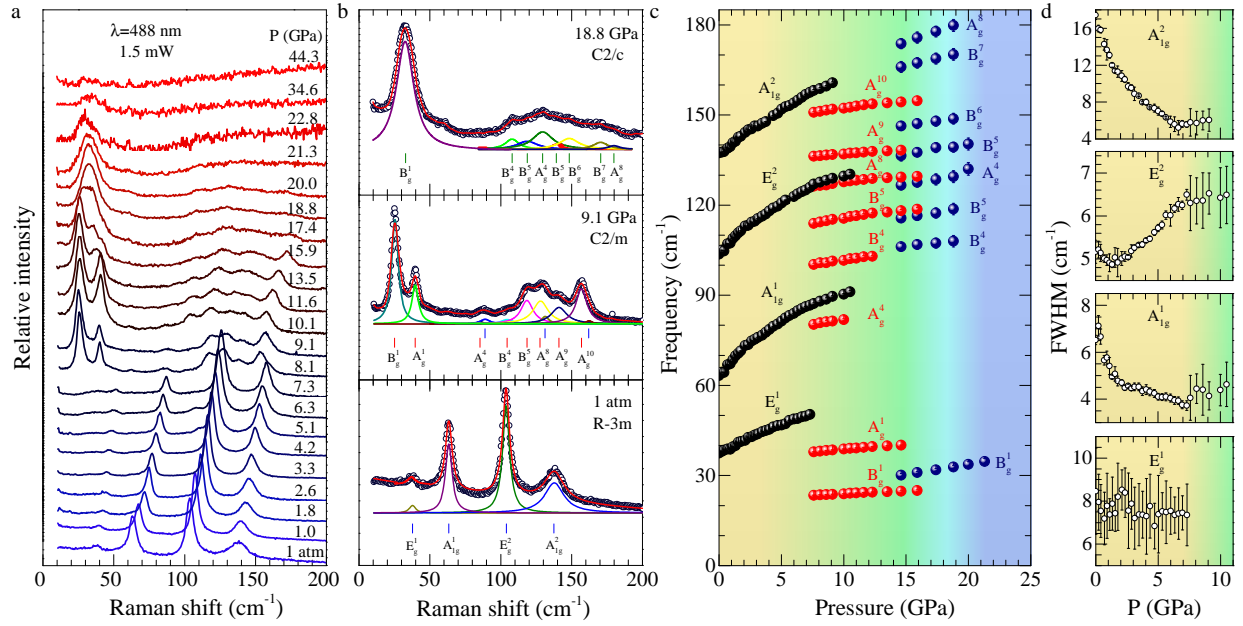
64. Zhu, H. L., Dong, J. C., Li, P. S., Wang, Y., Guo, Z. Y., Shan, X. M., Gong, Y., An, P. F., Li, X. D., Zhang, J. & Chen, D. L. Bi-centric view of the isostructural phase transitions in α -Bi₂Se₃ and α -Bi₂Te₃. *Phys. Status Solidi B* **254**, 1700007 (2017).
65. Ma, Y. M., Liu, G. T., Zhu, P. W., Wang, H., Wang, X., Cui, Q. L., Liu, J. & Ma, Y. M. Determinations of the high-pressure crystal structures of Bb₂Te₃. *J. Phys.: Condens. Matter* **24**, 475403 (2012).
66. Bera, A., Pal, K., Muthu, D. V. S., Sen, S., Guptasarma, P., Waghmare, U. V. & Sood, A. K. Sharp Raman anomalies and broken adiabaticity at a pressure induced transition from band to topological insulator in Sb₂Se₃. *Phys. Rev. Lett.* **110**, 107401 (2013).
67. Sologub, V. V., Shubnikov, M. L., Itskevich, E. S., Kashirskaya, L. M., Parfen'ev, R. V. & Goletskaya, A. D. Change of Bi₂Te₃ band structure under hydrostatic compression. *Sov. Phys. JETP* **52**, 1203-1206 (1980).
68. Abrikosov, A. A. Fundamentals of the theory of metals, North-Holland, Amsterdam, 1988.
69. Suslov, I. M. Peculiarities of the drag-induced thermoelectric power at the topological transition points. *JETP Lett.* **46**, 30-32 (1987).
70. Blanter, Ya. M., Kaganov, M. I., Pantsulaya, A. V. & Varlamov, A. A. The theory of electronic topological transitions. *Phys. Rep.* **245**, 159-257 (1994).
71. Itskevich, E. S., Kashirskaya, L. M. & Kraidenov, V. F. Anomalies in the low-temperature thermoelectric power of p -Bi₂Te₃ and Te associated with topological electronic transitions under pressure. *Semiconductors* **31**, 276-278 (1997).

72. Khvostantsev, L. G., Orlov, A. I., Abrikosov, N. Kh., Svechnikova, T. E. & Chizhevskaya, S. N. Thermoelectric properties and phase transitions in Bi_2Te_3 under hydrostatic pressure up to 9 GPa and temperature up to 300 °C. *Phys. Status Solidi A* **71**, 49-53 (1982).
73. Ovsyannikov, S. V., Shchennikov, V. V., Vorontsov, G. V., Manakov, A. Y., Likhacheva, A. Y. & Kulbachinskii, V. A. Giant improvement of thermoelectric power factor of Bi_2Te_3 under pressure. *J. Appl. Phys.* **104**, 053713 (2008).
74. Zhang, J. K., Liu, C. L., Zhang, X., Ke, F., Han, Y. H., Peng, G., Ma, Y. Z. & Gao, C. X. Electronic topological transition and semiconductor-to-metal conversion of Bi_2Te_3 under high pressure. *Appl. Phys. Lett.* **103**, 052102 (2012).
75. Einaga, M., Tanabe, Y., Nakayama, A., Ohmura, A., Ishikawa, F. & Yamada, Y. New superconducting phase of Bi_2Te_3 under pressure above 11 GPa. *J. Phys.: Conf. Ser.* **215**, 012036 (2010).
76. Kong, P. P., Zhang, J. L., Zhang, S. J., Zhu, J., Liu, Q. Q., Yu, R. C., Fang, Z., Jin, C. Q., Yang, W. G., Yu, X. H., Zhu, J. L. & Zhao, Y. S. Superconductivity of the topological insulator Bi_2Se_3 at high pressure. *J. Phys.: Condens. Matter* **25**, 362204 (2013).
77. Zhang, C., Sun, L. L., Chen, Z. Y., Zhou, X. J., Wu, Q., Yi, W., Guo, J., Dong, X. L. & Zhao, Z. X. Phase diagram of a pressure-induced superconducting state and its relation to the Hall coefficient of Bi_2Te_3 single crystals. *Phys. Rev. B* **83**, 140504(R) (2011).
78. Zhang, S. J., Zhang, J. L., Yu, X. H., Zhu, J., Kong, P. P., Feng, S. M., Liu, Q. Q., Yang, L. X., Wang, X. C., Cao, L. Z., Yang, W. G., Wang, L., Mao, H. K., Zhao, Y. S., Liu, H. Z.,

- Dai, X., Fang, Z., Zhang, S. C. & Jin, C. Q. The comprehensive phase evolution for Bi_2Te_3 topological compound as function of pressure. *J. Appl. Phys.* **111**, 112630 (2012).
79. Matsubayashi, K., Terai, T., Zhou, J. S. & Uwatoko, Y. Superconductivity in the topological insulator Bi_2Te_3 under hydrostatic pressure. *Phys. Rev. B* **90**, 125126 (2014).
80. Zhang, H. J., Liu, C. X., Qi, X. L., Dai, X., Fang, Z. & Zhang, S. C. Topological insulators in Bi_2Se_3 , Bi_2Te_3 and Sb_2Te_3 with a single Dirac cone on the surface. *Nat. Phys.* **5**, 438-442 (2009).
81. Hohenberg, P. & Kohn, W. Inhomogeneous electron gas. *Phys. Rev. B* **136**, 864-871 (1964).
82. Kohn, W. & Sham, L. J. Self-consistent equations including exchange and correlation effects. *Phys. Rev. A* **140**, 1133-1138 (1965).
83. Kresse, G. & Hafne, J. Ab initio molecular dynamics for liquid metals. *Phys. Rev. B* **47**, 558-561(R) (1993).
84. Kresse, G. & Hafner, J. Ab initio molecular-dynamics simulation of the liquid-metal amorphous-semiconductor transition in germanium. *Phys. Rev. B* **49**, 14251-14269 (1994).
85. Kresse, G. & Furthmüller, J. Efficient iterative schemes for ab initio total-energy calculations using a plane-wave basis set. *Phys. Rev. B* **54**, 11169-11186 (1996).
86. Perdew, J. P., Burke, K. & Ernzerhof, M. Generalized gradient approximation made simple. *Phys. Rev. Lett.* **77**, 3865-3868 (1996).

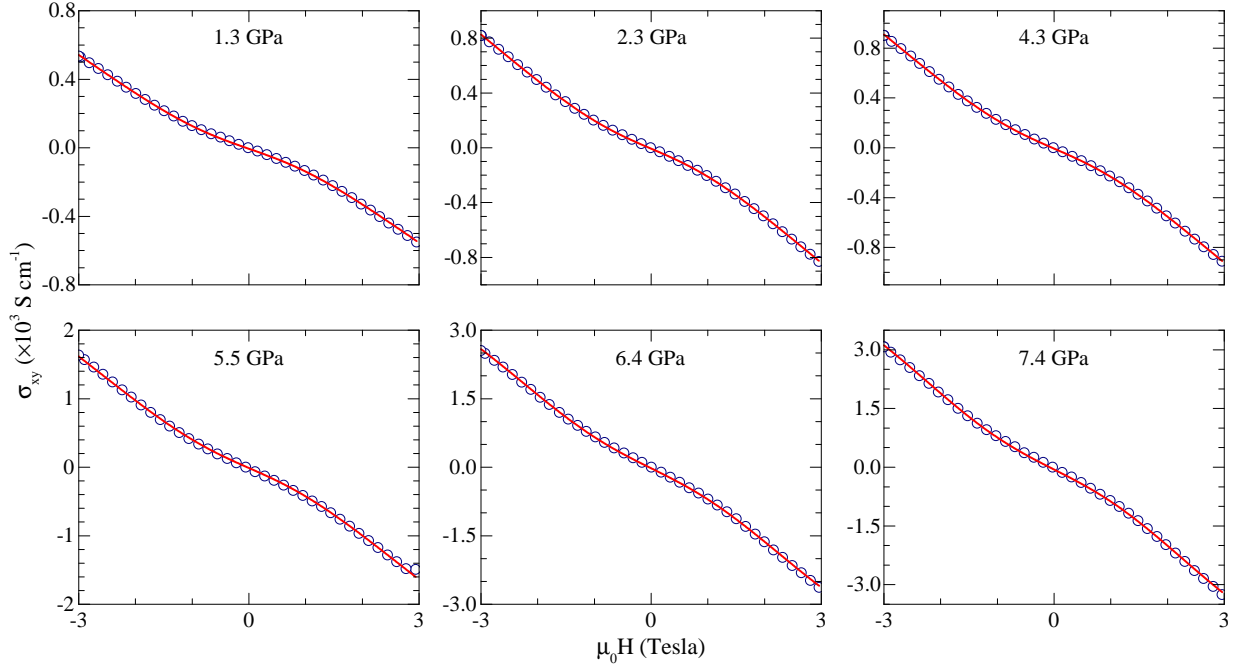
Extended Data Table 1 | Detailed structural parameters of Bi₂Te_{2.7}Se_{0.3} at room temperature.

P (GPa)	Space group	Lattice parameters	Atom	Site	<i>x</i>	<i>y</i>	<i>z</i>
1.0	<i>R</i> -3 <i>m</i>	<i>a</i> =4.391(3) Å	Bi	6 <i>c</i>	0	0	0.4080(1)
		<i>c</i> =30.482(27) Å	Te/Se(1)	6 <i>c</i>	0	0	0.3524(1)
		<i>R_p</i> =1.6%, <i>R_{wp}</i> =2.2%	Te/Se(2)	3 <i>a</i>	0	0	0
13.3	<i>C</i> 2/ <i>m</i>	<i>a</i> =14.624(20) Å	Bi(1)	4 <i>i</i>	0.1654(3)	0	0.1903(7)
		<i>b</i> =4.032(4) Å	Bi(2)	4 <i>i</i>	0.4498(9)	0	0.2323(2)
		<i>c</i> =17.243(19) Å	Te/Se(1)	4 <i>i</i>	0.2356(5)	0	0.4047(8)
		<i>β</i> =148.229(21) °	Te/Se(2)	4 <i>i</i>	0.0098(6)	0	0.5745(7)
		<i>R_p</i> =1.7%, <i>R_{wp}</i> =2.3%	Te/Se(3)	4 <i>i</i>	0.3352(1)	0	0.9808(8)
20.6	<i>C</i> 2/ <i>c</i>	<i>a</i> =10.145(29) Å	Bi	8 <i>f</i>	0.2586(6)	0.1155(4)	0.8333(4)
		<i>b</i> =6.728(13) Å	Te/Se(1)	8 <i>f</i>	0.6013(5)	0.3709(9)	0.9777(5)
		<i>c</i> =10.467(26) Å	Te/Se(2)	4 <i>e</i>	0	0.5946(9)	0.25
		<i>β</i> =134.373(39) °					
		<i>R_p</i> =7.5%, <i>R_{wp}</i> =8.8%					
28.0	<i>I</i> <i>m</i> -3 <i>m</i>	<i>a</i> =3.611(16) Å	Bi	2 <i>a</i>	0	0	0
		<i>R_p</i> =7.2%, <i>R_{wp}</i> =7.4%	Te/Se	2 <i>a</i>	0	0	0

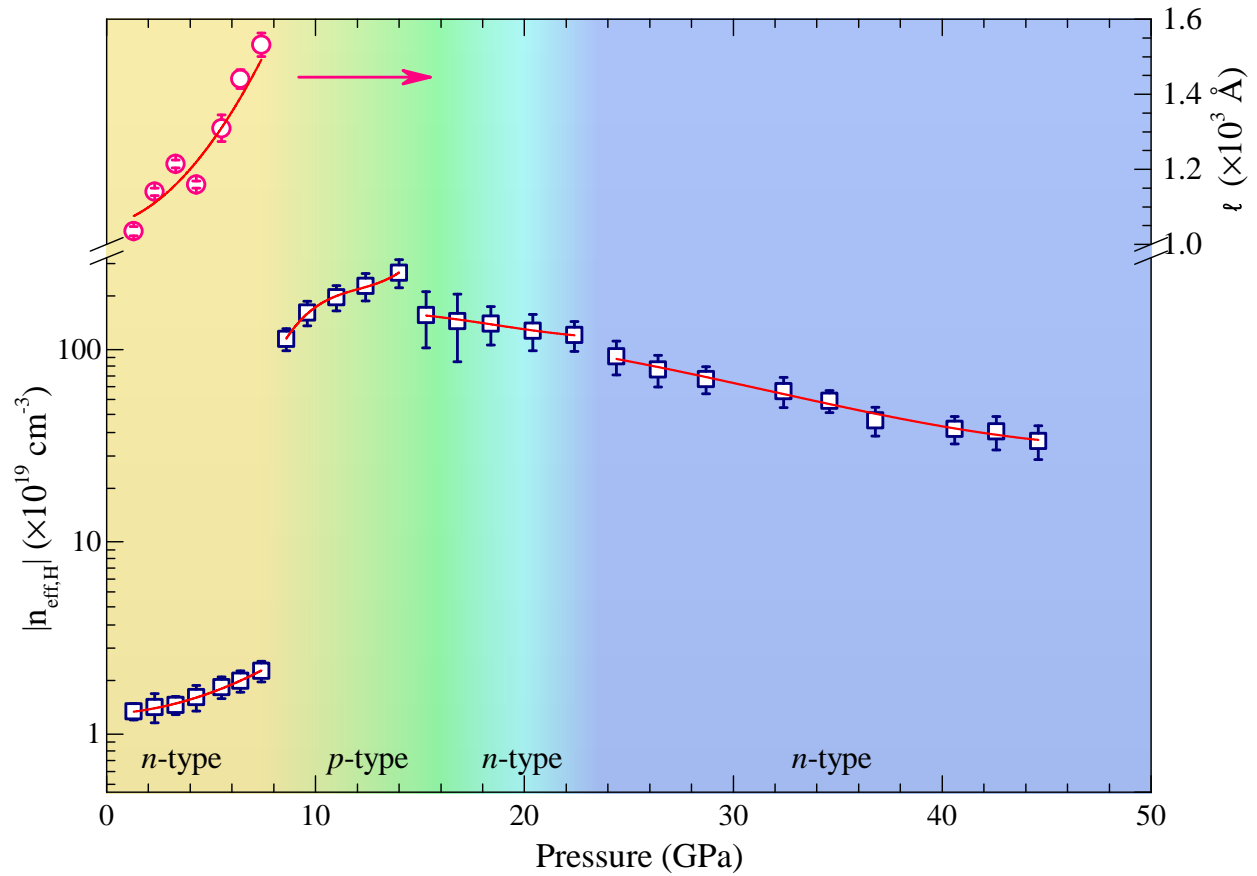


Extended Data Fig. 1 | High-pressure vibrational properties of $\text{Bi}_2\text{Te}_{2.7}\text{Se}_{0.3}$ at room temperature. **a**, Raman scattering spectra collected at various pressures up to 44.3 GPa at room temperature with the laser excitation of 488 nm and laser power of 1.5 mW. The spectra change profiles at pressures of 8.1 and 17.4 GPa. No active Raman peaks at higher pressures above 22.8 GPa are observed. **b**, From the bottom to top, Representative Raman spectra in open cycles for the phase with space group of $R-3m$ at ambient pressure, $C2/m$ at 9.2 GPa, and $C2/c$ at 18.2 GPa, respectively. Lorentz fitting to the data points is shown in the curve for individual phonon mode and their combination. The sticks at each bottom denote the calculated frequencies of the Raman-active modes for the corresponding structure symmetry. **c**, Pressure dependence of the frequency of each phonon mode in the first three phases with the space group of $R-3m$ (Phase I), $C2/m$ (Phase II), and $C2/c$ (Phase III), respectively. The regime for each phase, the boundary in between of them, and their coexistence can be judged from the data points. **d**, Pressure dependence of FWHM of the

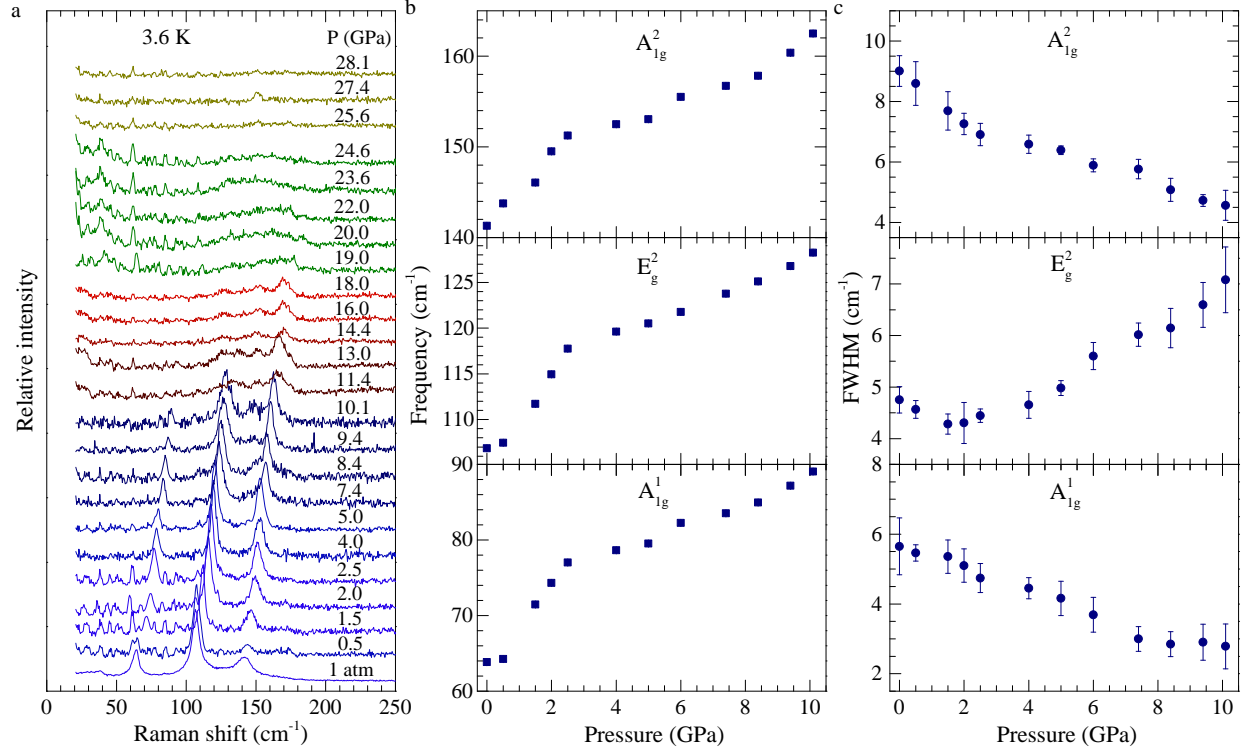
phonon mode E_g^1 , A_{1g}^1 , E_g^2 , and A_{1g}^2 (from the bottom to top) for the Phase I with the space group of $R-3m$. There is a maximum (minimum) for the E_g^1 (E_g^2) mode at a pressure close to 2 GPa at which the A_{1g}^1 and A_{1g}^2 mode changes curvature.



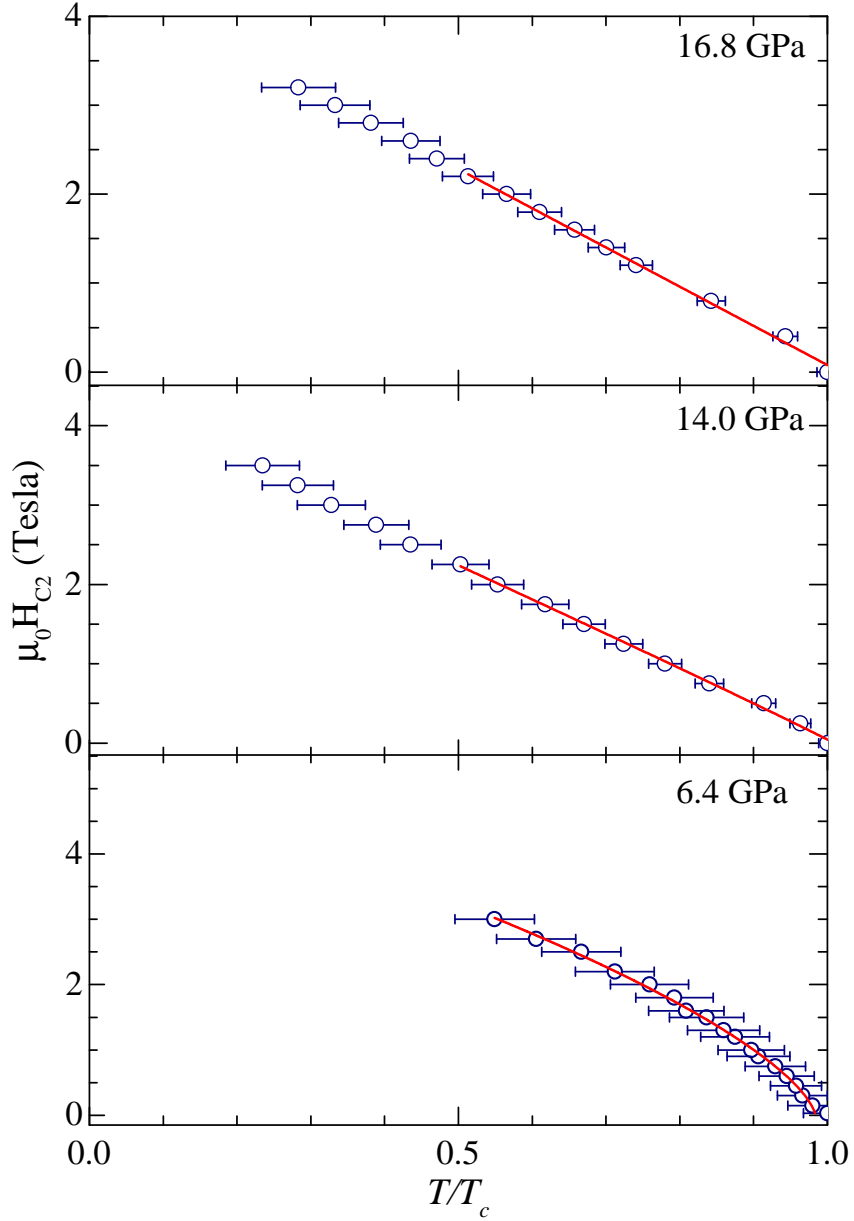
Extended Data Fig. 2 | Hall conductivity σ_{xy} vs applied magnetic field for $\text{Bi}_2\text{Te}_{2.7}\text{Se}_{0.3}$. The data were taken for Phase I with the space group of $R\bar{3}m$ at selected pressures and at temperature of 10 K. The open cycles are the experimental data points. The curves are the fitting results to the experiments by considering the combination effects from the bulk and surface states.



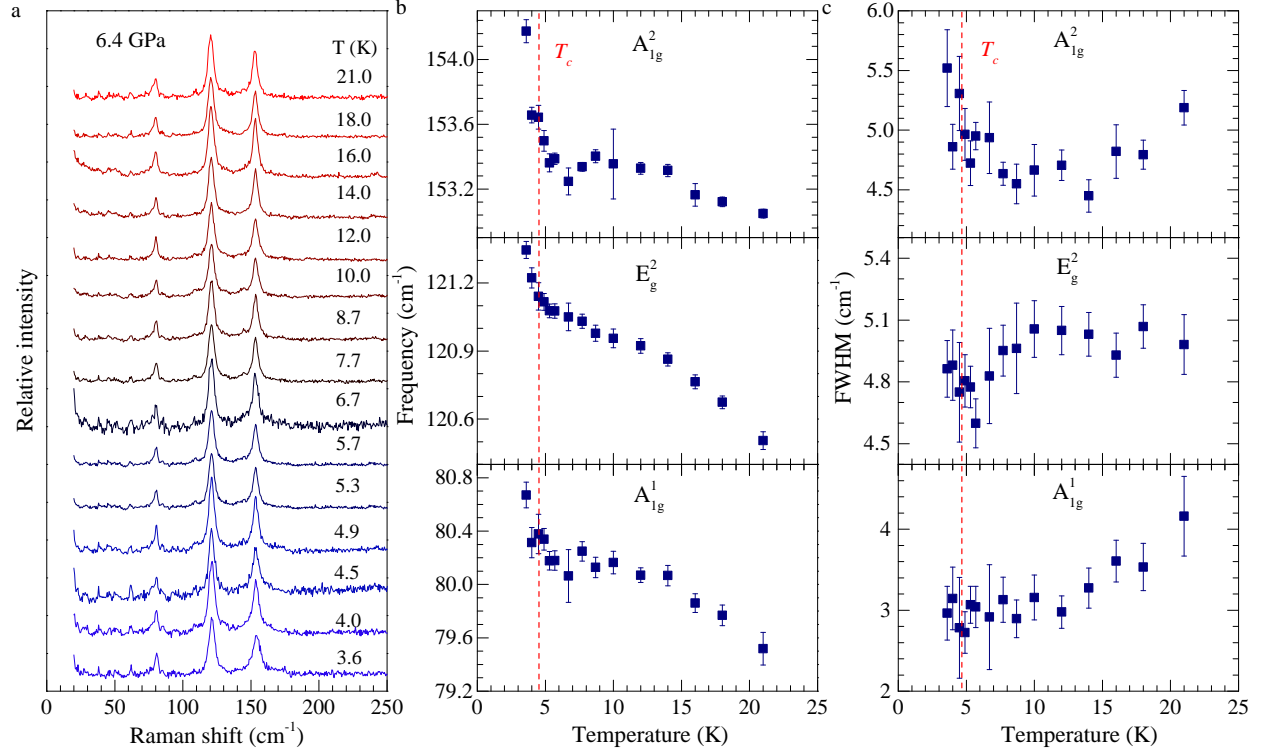
Extended Data Fig. 3 | Pressure dependence of the bulk carrier concentration in the absolute value for $\text{Bi}_2\text{Te}_{2.7}\text{Se}_{0.3}$ at temperature of 10 K. Left panel: The effective carrier concentration n_{eff} of the bulk in Phase I and the bulk carrier concentration n_H of the rest phases. Right panel: Mean free path l of Phase I. The line is drawn for the guide to the eye. The material is n -type in Phase I, III, IV but p type in Phase II. This character can be judged from Fig. 2a.



Extended Data Fig. 4 | Evolution of the phonon modes with pressure for $\text{Bi}_2\text{Te}_{2.7}\text{Se}_{0.3}$ at temperature of 3.6 K. **a**, Low-temperature Raman spectra at various pressures up to 28.1 GPa. Four phases can be identified from the different profiles of their phonon modes. In the superconducting state of each phase, the Raman spectra have the same profiles compared with the normal state at the room temperature (Extended Data Fig. 1). This indicates that the superconducting phase carries on all the features of this phase at the normal state. The first superconducting phase thus keeps its nontrivial topological order. **b** and **c**, Pressure dependence of the frequency and FWHM of the A_{1g}^1 , E_g^2 , and A_{1g}^2 mode in Phase I with the space group of $R-3m$.



Extended Data Fig. 5 | Enlarged view of the upper critical field as a function of the reduced temperature (T/T_c) of $\text{Bi}_2\text{Te}_{2.7}\text{Se}_{0.3}$ at selected pressures. The experimental data are represented by open cycles. The fitting to the experimental data points near T_c in the T/T_c range of 0.5 to 1 is shown in the curve by using $\mu_0 H_{c2} \sim (1 - T/T_c)^\alpha$ with α of 2/3 for pressure of 6.4 GPa and of 1.0 for pressure of 14.0 and 16.8 GPa, respectively.



Extended Data Fig. 6 | Temperature-dependent Raman spectra for $\text{Bi}_2\text{Te}_{2.7}\text{Se}_{0.3}$ across the superconducting transition in Phase I at pressure of 6.4 GPa. a, Raman spectra at low temperatures down to 3.6 K. **b and c,** Temperature dependence of the frequency and FWHM of the A_{1g}^1 , E_g^2 , and A_{1g}^2 mode. The T_c is indicated by the dashed line.